Nanoscale domain patterns and a concept for an energy harvester

Ananya Renuka Balakrishna and John E Huber

Department of Engineering Science, University of Oxford - OX1 3PJ, UK

Email: john.huber@eng.ox.ac.uk

Abstract. The current work employs a phase-field model to test the stability of nanoscale periodic domain patterns, and to explore the application of one pattern in an energy harvester device. At first, the stability of several periodic domain patterns with in-plane polarizations is tested under stress-free and electric field-free conditions. It is found that simple domain patterns with stripe-like features are stable, while patterns with more complex domain configurations are typically unstable at the nanoscale. Upon identifying a stable domain pattern with suitable properties, a conceptual design of a thin film energy harvester device is explored. The harvester is modelled as a thin ferroelectric film bound to a substrate. In the initial state a periodic stripe domain pattern with zero net charge on the top electrode is modelled. On bending the substrate, a mechanical strain is induced in the film, causing polarized domains to undergo ferroelectric switching and thus generate electrical energy. The results demonstrate the working cycle of a conceptual energy harvester which, on operating at kHz frequencies, such as from vibrations in the environment, could produce an area power density of about 40W/m^2.

1. Introduction

Ferroelectric materials possess spontaneous polarization in unit cells that can be reoriented by the application of an electric field or mechanical stresses [1]. This reorientation of polarization is typically accompanied by a change in surface charge distribution that finds applications in sensors [2], [3], energy harvesters [4]–[6] and memory elements [7], [8]. A typical ferroelectric contains nanoscale regions of uniform polarization referred to as domains, which fit compatibly together to form polarization patterns [9]–[11]. These polarization patterns are important to the working of nanoscale or thin film based devices where the length scale is comparable to the domain size [3], [12]–[14], and the domain configurations can be engineered to improve ferroelectric properties [15], [16].

Several designs of nanoscale ferroelectric energy harvesters are proposed that generate sizeable amount of power [5], [17], [18]. However, these devices typically contain nanoscale features which pose fabrication difficulties [5], [17] or require a complex configuration of domains in the initial state [5]. Here, we model an energy harvester comprising a monocrystalline ferroelectric thin film bound to conductive substrate, a relatively simple configuration to manufacture. With technological advances in thin film fabrication [19]–[21], film thickness of the order of $10nm$ nanometres are achievable [19], [22], [23]. In the present work we consider a 40nm film with a simple alternating configuration of domains that is commonly found in thin films [24]–[26].

Phase-field models have been employed to simulate nanoscale properties of ferroelectrics [27], [28] and ferromagnetics [29] as well as to explore their application in nanoscale devices [27], [30], [31]. They offer great advantages in tracking domain walls [28]. Baek et al. [29] used phase-field simulations to demonstrate the stabilisation of ferroelastic switching in $BiFeO_3$, which has applications in non-volatile magnetoelectric devices. Similarly Balke et al. [27], employed phase-field simulations to illustrate enhanced electric conductivity at $BiFeO_3$ vortex cores, thereby indicating their potential application in integrated oxide electronic devices. Here, we employ a phase-field model [32], [33] that has been established for studying the behaviour of barium titanate.

In this paper, we first use a phase-field model to assess several nanoscale periodic polarization patterns and then explore a conceptual design of an energy harvester. Tsou et al. [34]

2

identified several periodic polarization patterns that can form in tetragonal ferroelectrics and possess useful functional properties. However, on testing the stability of these polarization patterns it is found that most become unstable when the domains are a few nanometres in size. By contrast, a simpler, layered pattern is found to be stable, and allows the domain walls to sweep back and forth under external loads. Therefore, we explore the potential application of this pattern in an energy harvester device. Here, a thin film of BaTiO$_3$ with stripe domain pattern is modelled with plane strain and plane electric field conditions on a conductive substrate. Mechanical loads are applied to the film by substrate bending that causes polarization switching in the stripe domain pattern. Using phase-field simulations we demonstrate the working cycle of the energy harvester device and find a potential area power density of up to 40W/m^2, at an operating frequency of 1kHz. This is comparable with the power density of currently available photovoltaic cells, and greater than typical piezoelectric vibration harvesters, making the concept attractive for further development.

2. Phase-field model

We give only the briefest review of the phase-field model used for the current study, as its details have been reported elsewhere, by Landis and co-workers [32], [33]. In this model, the volumetric Helmholtz free energy, ψ is described by:

$$\psi = \frac{1}{2} a_{ijkl} P_{i,j} P_{k,l} + \frac{1}{2} \bar{a}_{ij} P_i P_j + \frac{1}{4} \bar{\bar{a}}_{ijkl} P_i P_j P_k P_l$$

$$+ \frac{1}{6} \bar{\bar{\bar{a}}}_{ijklmn} P_i P_j P_k P_l P_m P_n + \frac{1}{8} \bar{\bar{\bar{\bar{a}}}}_{ijklmnrs} P_i P_j P_k P_l P_m P_n P_r P_s$$

$$+ b_{ijkl} \varepsilon_{ij} P_k P_l + \frac{1}{2} c_{ijkl} \varepsilon_{ij} \varepsilon_{kl} + \frac{1}{2} f_{ijklmn} \varepsilon_{ij} \varepsilon_{kl} P_m P_n$$

$$+ \frac{1}{2} g_{ijklmn} \varepsilon_{ij} P_k P_l P_m P_n + \frac{1}{2\kappa_0} (D_i - P_i)(D_i - P_i) \tag{1}$$

Here ψ is a function of polarization P_i, polarization gradient $P_{i,j}$, strain ε_{ij} and electric displacement D_i. In Eq. (1) the first term accounts for the domain wall energy, while the remaining terms contribute to the bulk energy of the ferroelectric system. Further details on the tensorial coefficients

3

$\mathbf{a}, \overline{\mathbf{a}} \dots \overline{\overline{\overline{\mathbf{a}}}}, \mathbf{b}, \mathbf{c}, \mathbf{f}$ and $\mathbf{g}$, and the material properties can be found in refs. [32], [33]. The model is calibrated for barium titanate and is solved for equilibrium using the time dependent Ginzburg-Landau equation [32]:

$$\left(\frac{\partial \psi}{\partial P_{i,j}}\right)_{,j} - \frac{\partial \psi}{\partial P_i} = \beta \dot{P}_i. \qquad (2)$$

The relaxation parameter β is used to find equilibrium states, which are then confirmed by solving the system equations with $\beta = 0$. This phase-field model is first used to test the stability of several periodic domain patterns with a view to identifying stable domain patterns with useful energy harvesting properties.

3. Periodic domain patterns and their stability

The objective is to identify a periodic pattern of domains that has useful properties for energy harvesting. This is achieved by first testing the stability of various known periodic domain patterns under conditions of zero average stress and electric field to see which, if any, are likely to be usable at the nanoscale. The candidate patterns are next tested under cyclic straining to see which remain stable and can provide a mechanically induced cyclic switching effect.

Planar domain patterns are modelled in 2-dimensions on a periodic square region of side $L = 40$nm, with plane strain and plane electric field conditions. The imposed boundary conditions allow the model to adopt states that are free of average stress or electric field. This is achieved by relating the displacement, electric potential and polarization values on typical boundary nodes indicated in figure 1.

Referring to figure 1, a mid-element of the periodic square is simply supported and the boundary nodes are modelled with periodic conditions. The boundary nodes are of two types, namely master nodes (such as P on edge AC or Q on edge AB) and dependent nodes (represented by R and S). A representative example of the periodic boundary conditions on the dependent nodes is:

$$u_i(L, x_2)\big|_R - u_i(L, 0)\big|_B = u_i(0, x_2)\big|_P - u_i(0, 0)\big|_A$$

$$\phi(L, x_2)\big|_R = \phi(0, x_2)\big|_P$$

4

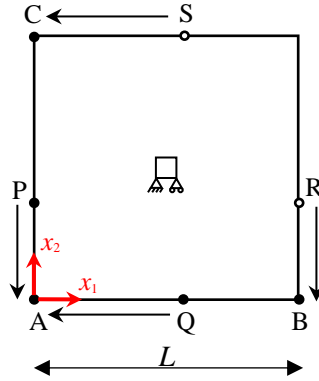$$P_i(L, x_2)\big|_R = P_i(0, x_2)\big|_P \qquad (3)$$

Figure 1: Schematic representation of boundary conditions on square region barium titanate of side, L. Arrows indicate nodal connectivity in periodic boundary conditions in equation (3).

where u_i is the displacement, ϕ is the electric potential and P_i is the polarization at each node. A similar set of periodic boundary condition is applied on the representative node 'S' [35]. These constraints enforce periodicity of the strain fields with zero average stress, and periodicity of the electric potential values with zero average electric field. Periodicity of polarization is also imposed at the boundary nodes. The boundary conditions given by equation (3) are referred in this paper as the zero external load conditions.

In the initial state of each simulation, polarization values corresponding to a known periodic pattern of domains are imposed on each node of the periodic square with sharp domain boundaries, see figure 2(a-e). This initial state is next allowed to relax towards equilibrium with slow stepping down of β values to reach equilibrium at $\beta = 0$. If the pattern persists at equilibrium then it is stable, suggesting that the pattern could form with domain wall spacings of order a few nm.

The stripe domain pattern, figure 2(a) and the herringbone domain pattern, figure 2(b) are found to be stable at equilibrium, while all the other patterns shown dissolved into either single domain states or a simple stripe pattern. The energy of each polarization pattern, and the associated strain and stress fields have been discussed in previous work [35] where it was found that the stripe

and herringbone pattern are stable due to the absence of stressed domains. Each of the other patterns are stressed due to incompatible domain junctions that increase their elastic energy.
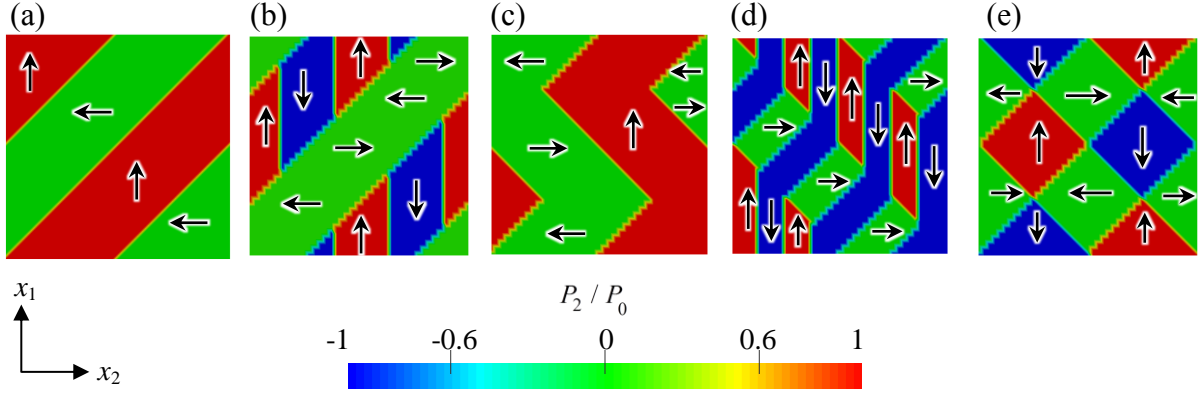

Figure 2: Establishing the stability of periodic domain patterns (a) stripe (b) herringbone (c) herringbone-monodomain (d) herringbone-stripes and (e) checkerboard, under stress-free and electric field-free boundary conditions. $P_0 = 0.26\text{C/m}^2$, is the spontaneous polarization of BaTiO$_3$.

Next, the stability of the two candidate patterns, herringbone and stripe domains, is explored under external mechanical loading in the form of compressive strain, ε_{11} imposed by a substrate. The stability of the domain pattern under an external strain field is a useful property for the energy harvester device, which generates electrical energy from mechanical loads. Here, a uniform strain ε_{11} is imposed by displacing the nodes along $x_2 = 0$ of the periodic cell, while the boundary conditions for nodes along $x_1 = 0$ and $x_1 = L$ remain periodic, as given by equation (3).

A small axial strain $\varepsilon_{11} = 0.1\varepsilon_0$, where $\varepsilon_0 = 0.0082$ is the spontaneous strain of BaTiO$_3$, was found to destabilize the herringbone pattern causing the domains to merge together at equilibrium. This pattern did not undergo cyclic polarization switching and so appeared unsuitable for energy harvesting. By contrast, the stripe domain pattern was stable over a wide range of imposed strain, $0 \leq \varepsilon_{11} \leq 0.65\varepsilon_0$. The width of the stripes in this domain pattern changes in proportion to the applied strain. However the overall domain configuration remains the same; this aspect is discussed in detail in section 4. This feature of cyclic switching with domain walls sweeping back and forth but

6

remaining in the same pattern appears promising for energy harvesting. Previous works indicate that applied stresses [36] and imposed substrate strains [37] initiate the 90° ferroelastic domain wall movement in polarization patterns. We next explore the effect of domain wall position within the stripe domain pattern by changing the separation distance l_w of
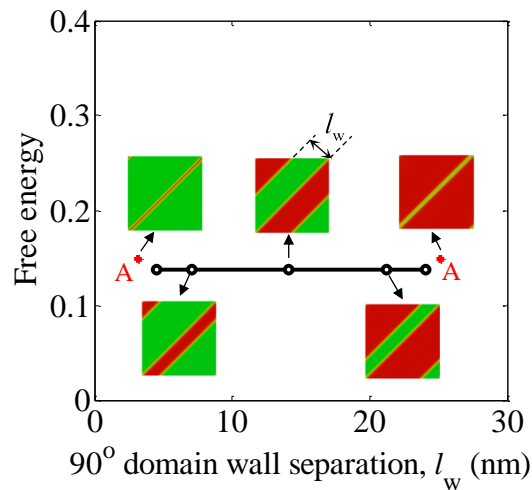

Figure 3: The volume average free energy (normalized [35]) of the stripe domain pattern as a function of domain wall separation, l_w. Inset schematics denote polarization patterns. The solid line connects the free energy of domain patterns at equilibrium, while the markers 'A' at the far end of the plots indicate the free energy of unstable domain patterns before collapse into a monodomain at equilibrium.

adjacent domain walls, while keeping the size of the periodic cell constant. Here, we initialize the stripe domain pattern with varying separation distance l_w, under zero external load conditions, equation (3), and relax towards equilibrium. The volume average free energy is plotted as a function of separation distance in figure 3. The relaxation process produces no significant change in the domain pattern, apart from smoothing the domain walls. The free energy is almost independent of the domain wall separation for the stripe pattern, indicating that the domain walls are in a neutral equilibrium. When $l_w \sim 4\text{nm}$, the pattern is unstable and collapses to a monodomain. A symmetrically opposite state has $l_w \sim 25\text{nm}$ and also collapses. In these cases, the energy was

7

calculated before collapse (not in equilibrium) see markers 'A' at far ends in figure 3. The key result is that the stripe pattern is stable over a wide range of separation of domain walls and also under external mechanical loads, which motivates us to employ this pattern for designing an energy harvester concept.

4. Energy harvester concept

The proposed energy harvester concept is a device that cyclically converts input mechanical energy, in the form of stresses/substrate strains, into electrical energy. The concept is similar to existing designs of piezoelectric vibration energy harvesters, except that the device undergoes ferroelectric/ferroelastic switching during each cycle of operation. The harvester comprises a barium titanate thin film on a conductive substrate with a top electrode, see figure 4(a-c).
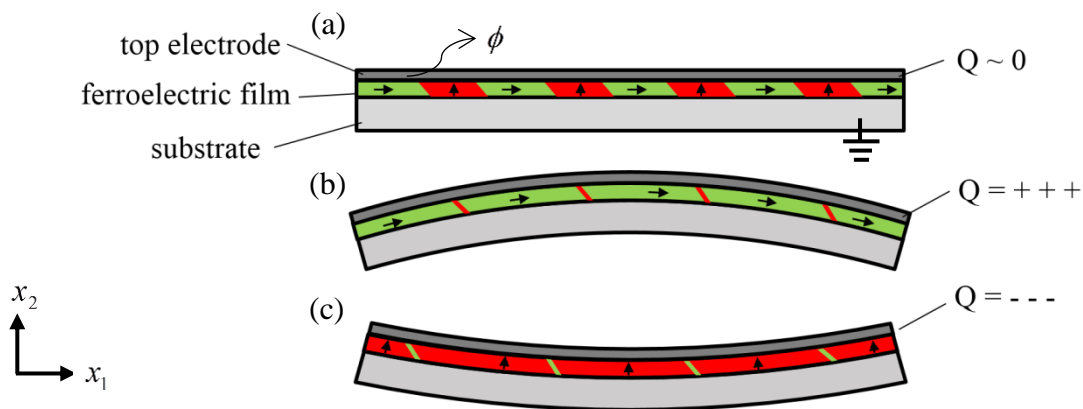

Figure 4(a-c): Schematic illustration of the working concept of the energy harvester

The top electrode is connected to an external circuit at a voltage ϕ, while the substrate is electrically grounded. The initial state is taken to be a stripe domain pattern with zero net charge on the top electrode (this is an arbitrary reference state for surface charge density). On bending the substrate, a mechanical strain is induced in the ferroelectric film, causing the polarized domains to switch. For example, in figure 4(b), tensile strain along the length of the ferroelectric film is expected to cause the domains with polarization aligned along the x_1 – axis to grow in size; conversely, compressing the film by reversing the sense of bending, see figure 4(c), causes the domains polarized

along the x_2 − axis to grow in size. This change in domain sizes drives a net electric charge onto or off the top electrode, enabling electrical work to be done in an external circuit. Now, if voltage ϕ is maintained constant throughout the cycle, then charge flows onto and off the top electrode at the same voltage and no net electrical work is done. Instead, suppose that during the compressive part of the cycle, voltage $\phi = 0$ so that charge flows off the electrode without electrical work, and then ϕ is switched to a negative value for the tensile part of the cycle. In this case the tensile part of the cycle drives charge against a negative voltage and electrical work can be extracted. Such an operation requires external energy harvesting circuitry that will switch the electrode voltage in phase with the mechanical vibration cycle. We return to this aspect later in this section.

To model the energy harvester concept, a square periodic cell of BaTiO$_3$ is simulated with plane strain and electric field conditions, see figure 5. A cell with side $L = 40$nm is chosen, noting that at this size the domain spacing in the stripe domain pattern is about $l_w = 14$nm and the domain walls have freedom to move without the pattern collapsing into a monodomain. An axial in-plane strain, ε_{11}, is induced by the conductive substrate and modelled by imposing nodal displacements along the edge AB at $x_2 = 0$. At the top surface, $x_2 = L$ an electrode of area A is modelled by imposing voltage ϕ; for simplicity it is assumed that the electrode does not provide significant mechanical constraint. Nodes along $x_1 = 0$ and $x_1 = L$ are constrained with the periodic boundary conditions given by equation (3). The simulation is initialized by imposing a stripe pattern on the periodic cell with sharp interfaces. The voltage on the top electrode is set to $\phi = 0$ and the initially imposed substrate strain $\varepsilon_{11} = 0.3\varepsilon_0$ is applied at $x_2 = 0$. This choice of substrate strain matches the average strain of the unstressed stripe pattern with equal volume fractions of the two domain types, found in prior calculations. The periodic cell of the energy harvester is then solved using the phase-field model to
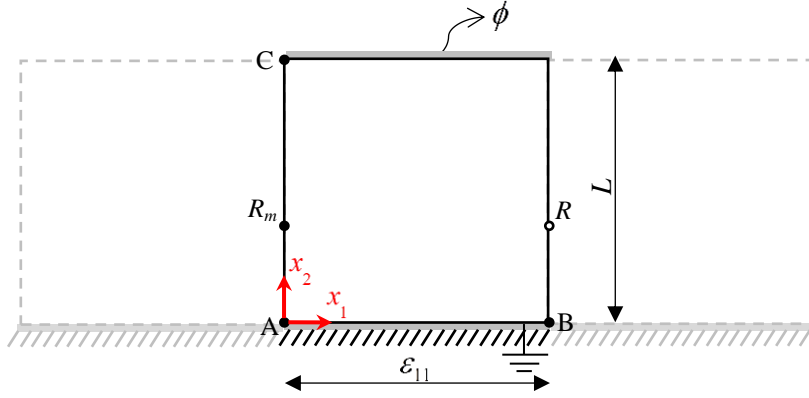
Figure 5: Schematic illustration of the boundary conditions on a periodic cell of the energy harvester.

find an equilibrium stripe-like pattern, see figure 6(a). At $\varepsilon_{11} = 0.3\varepsilon_0$ the domains in the periodic cell,

that are polarized along the $x_1 -$ axis (P_1 domains) and the $x_2 -$ axis (P_2 domains) are of equal sizes

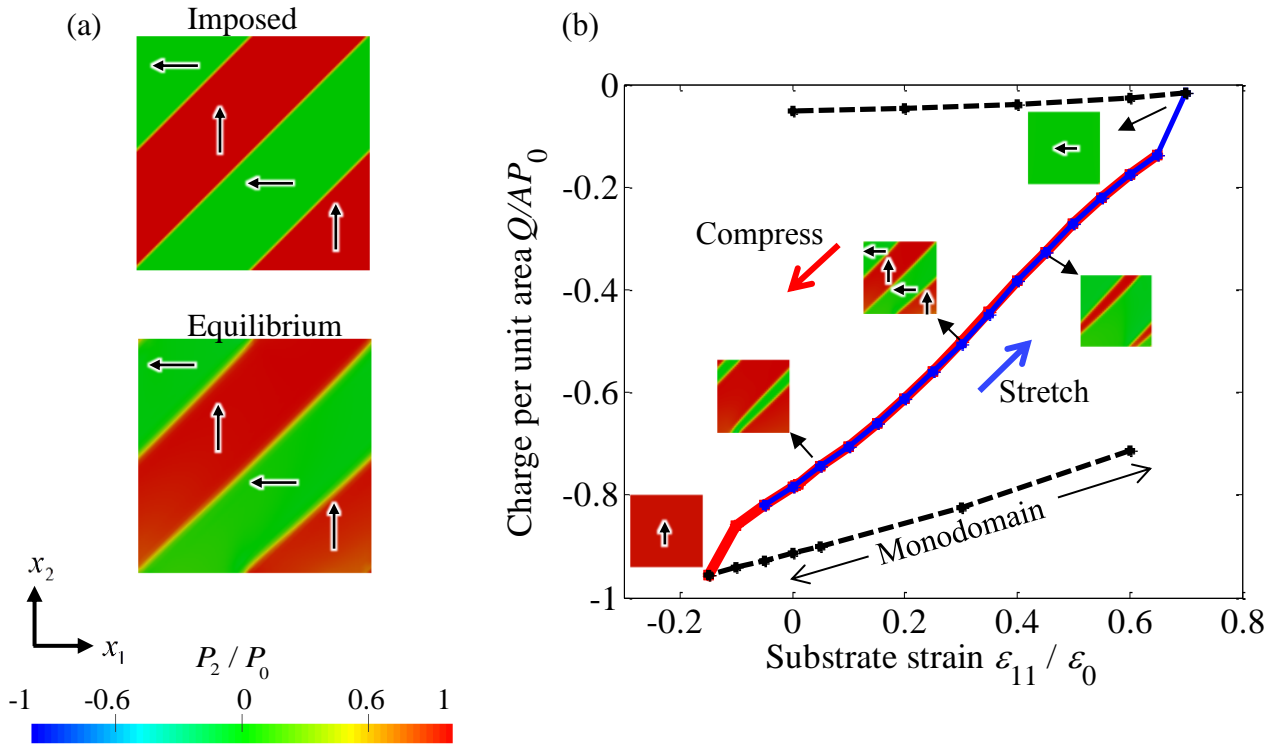and a net charge of $-0.13 \mathrm{C/m}^2$ is attracted onto the top electrode.

Figure 6: (a) Polarization pattern in the initial state of the energy harvester at $\varepsilon_{11} = 0.3\varepsilon_0$. (b) Charge

per unit area collected on the top electrode as a function of the substrate strain in the energy harvester.

A is the area of the top electrode and $P_0 = 0.26 \mathrm{C/m}^2$. The cycle is performed at $\phi = 0$ and inset

schematics illustrate the domain patterns polarized along the $x_2 -$ axis.

10

In order to achieve cyclic operation, it is necessary to limit the strain imposed by the substrate such that the film remains configured as a stripe pattern. If the substrate is strained too far, either in tension or in compression, a single domain state will be produced and the imposed periodicity of the pattern would be lost. To explore the tolerable limits of straining, a range of substrate strains was imposed while maintaining $\phi = 0$. Starting from the state with equal domain fractions, mechanical loading was applied to the energy harvester by incrementing the substrate strain in steps of $0.05\varepsilon_0$. In the first step the equilibrium domain pattern formed at $\varepsilon_{11} = 0.3\varepsilon_0$ is taken as the initial state and the substrate strain is increased to $0.35\varepsilon_0$. The system is then allowed to attain equilibrium. Subsequent steps increment or decrement the substrate strain in the range $-0.1\varepsilon_0 \le \varepsilon_{11} \le 0.7\varepsilon_0$, finding an equilibrium state at each step. The net charge per unit area collected on the top electrode is computed at each value of ε_{11} (with $\phi = 0$) and the results are shown in figure 6(b).

It can be seen from figure 6(b) that increasing the strain makes the net charge on the top electrode less negative. This is because the sizes of P_2 domains decrease with increasing ε_{11}, see inset schematics in figure 6(b). On compressing the substrate, the net charge on the top electrode becomes more negative. Significantly, for tensile substrate strains, $\varepsilon_{11} > 0.65\varepsilon_0$, or for compressive strains $\varepsilon_{11} < -0.1\varepsilon_0$, the stripe-like features in the periodic cell disappear leading to the formation of a uniformly polarized monodomain. Upon stretching/compressing the monodomain, the stripe-like features are not recovered, and the cycle is not repeatable. However, provided the substrate strain is limited to the range $0 \le \varepsilon_{11} \le 0.65\varepsilon_0$ a stable cycle occurs with domain walls sweeping back and forth through the film.

Next, the challenge is to extract electrical energy from a cycle of mechanical straining of the energy harvester. In order to achieve this, the voltage on the top electrode is varied during the energy harvester cycle, allowing electrical work to be extracted. An example of the energy harvester cycle is given in four steps, see table 1. The corresponding phase-field simulations are illustrated in figure 7.

The domain evolution through step AB, is illustrated by figure 7(a-d). Here, the voltage on the top electrode is held constant at $\phi = 0$, while the substrate strain is decreased in steps of $0.05\varepsilon_0$.

The P_2 domains grow and the charge on the top electrode changes as shown in figure 8(a). The portions of the domain walls in close proximity to the substrate curve due to the imposed strain, see figure 7(b). At point B, $\phi = 0$ and $\varepsilon_{11} = 0$, while the net charge per unit area on the top electrode is $\sim -0.8P_0$. Now, the substrate strain is briefly held constant at zero strain while the voltage on the top electrode is switched to -0.25V, step BC. During this step, further net charge per unit area of

Step	Voltage	Substrate strain	Charge per unit area
AB	Constant at $\phi = 0$	Decreased $\varepsilon_{11} = 0.65\varepsilon_0 \to 0$	$Q/A = -0.2P_0 \to -0.8P_0$
BC	Decreased to $\phi = -0.25\text{V}$	Constant at $\varepsilon_{11} = 0$	$Q/A = -0.8P_0 \to -0.9P_0$
CD	Constant at $\phi = -0.25\text{V}$	Increased $\varepsilon_{11} = 0 \to 0.65\varepsilon_0$	$Q/A = -0.9P_0 \to -0.35P_0$
DA	Increased to $\phi = 0$	Constant at $\varepsilon_{11} = 0.65\varepsilon_0$	$Q/A = -0.35P_0 \to -0.2P_0$

Table 1: Sequential steps in the energy harvester cycle. The steps A-B-C-D correspond to the plot in figure 8(a-b). Q/A is the net charge per unit area on the top electrode.

$\sim -0.1P_0$ flows on to the top electrode, and the domains polarized along x_2- axis grow slightly, see figure 7(d-e). In the subsequent step CD, the voltage on the top electrode is held constant at -0.25V and the substrate is stretched. Now the domains polarized along the direction of applied axial strain increase in size, see figure 7(f-i) changing the electrode charge to $\sim -0.35P_0$. At point D, with $\varepsilon_{11} = 0.65\varepsilon_0$, the substrate strain is again briefly held constant while the voltage switches back to 0V. This causes the charge per unit area to return to its initial state $\sim -0.2P_0$, see also figure 7(i-j). The energy harvester has now returned to its initial state, and the cycle can be repeated. The electrical work output per unit area in this cycle is $\sim 0.04\text{J/m}^2$.

(a) $\phi = 0$; $\varepsilon_{11} = 0.65\varepsilon_0$

(b) $\phi = 0$; $\varepsilon_{11} = 0.3\varepsilon_0$

(c) $\phi = 0$; $\varepsilon_{11} = 0.2\varepsilon_0$

(d) $\phi = 0$; $\varepsilon_{11} = 0$

(e) $\phi = -0.25\text{V}$; $\varepsilon_{11} = 0$

(f) $\phi = -0.25\text{V}$; $\varepsilon_{11} = 0.1\varepsilon_0$

(g) $\phi = -0.25\text{V}$; $\varepsilon_{11} = 0.2\varepsilon_0$

(h) $\phi = -0.25\text{V}$; $\varepsilon_{11} = 0.3\varepsilon_0$

(i) $\phi = -0.25\text{V}$; $\varepsilon_{11} = 0.65\varepsilon_0$

(j) $\phi = 0$; $\varepsilon_{11} = 0.65\varepsilon_0$

x_2

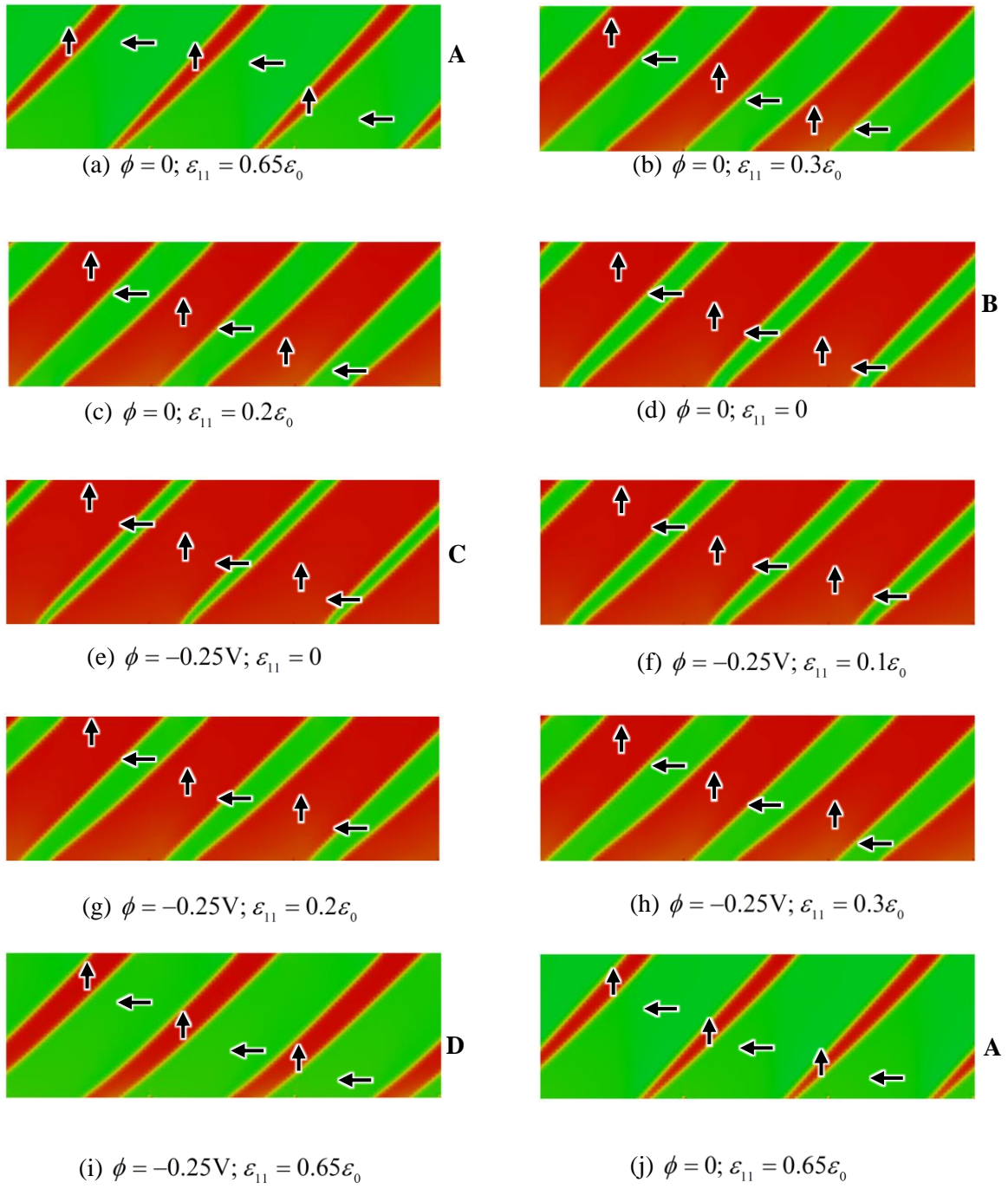x_1

P_2 / P_0

-1   -0.6   0   0.6   1

Figure 7(a-j): Domain patterns illustrating the working cycle of a conceptual energy harvester.
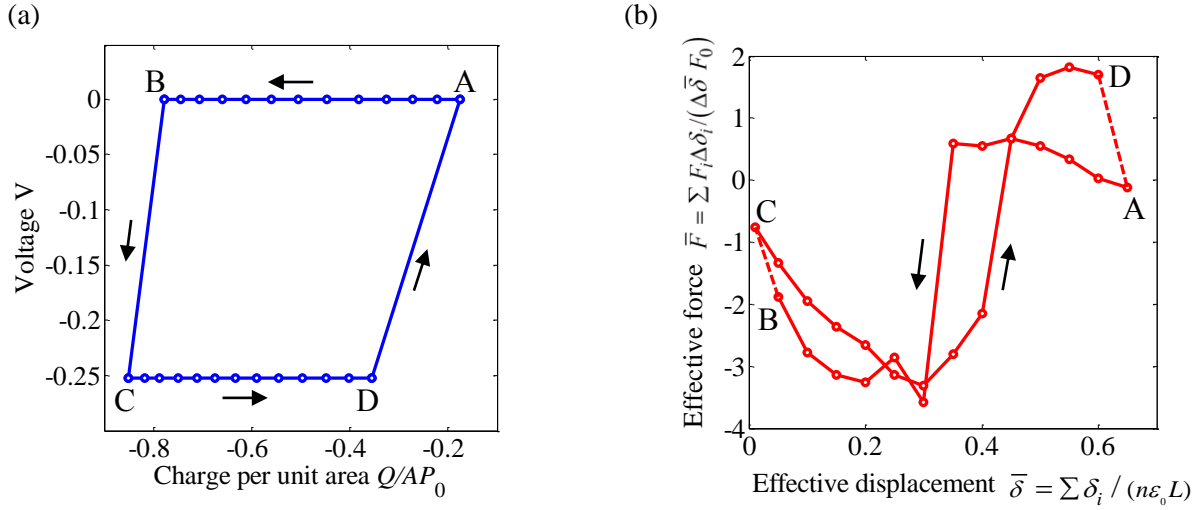
13

Figure 8: Plot of (a) voltage-charge (b) effective force-displacement in the energy harvester cycle shown in figure 7. $F_0 = 0.692\text{N/m}$.

An effective force-displacement curve for the energy harvester is plotted in figure 8(b). Here the effective displacement $\bar{\delta}$ is defined as a normalized average over the nodes on the substrate, $\bar{\delta} = \sum \delta_i / (n\varepsilon_0 L)$, where δ_i is the displacement of the ith node and n is the total number of substrate nodes. An effective force at the end of each step in the phase-field simulation is calculated by $\bar{F} = \sum F_i \Delta \delta_i / \Delta \bar{\delta} F_0$, where F_i is the nodal force value and the normalization for force per unit length is $F_0 = 0.692\text{N/m}$. This definition gives a work equivalent force such that the mechanical work increment in each step is $\bar{F} \Delta \bar{\delta}$. In figure 8(b), sharp transitions in effective force are observed on the curve segment AB upon decreasing $\bar{\delta} = 0.35 \rightarrow 0.30$, and likewise on the segment CD curve on increasing $\bar{\delta} = 0.40 \rightarrow 0.45$. These sharp transitions are caused by domain wall movements or polarization switching, $-P_1 \rightarrow P_2$ or $P_2 \rightarrow -P_1$, during the energy harvester cycle. Polarization switching is accompanied by a change in spontaneous strain values that affects the nodal forces. This abrupt change in nodal force is observed on each substrate node when a domain wall sweeps across it. The shape of the effective force-displacement curve is complicated. In figure 8(b), the primary contribution to the effective force, $\bar{F}$ arises from nodes closer to the edge of the periodic cell as $x_1 \rightarrow L$. This is because, for a given substrate strain, ε_{11} the the ith node is displaced as $\Delta \delta_i = \varepsilon_{11} x_1$.
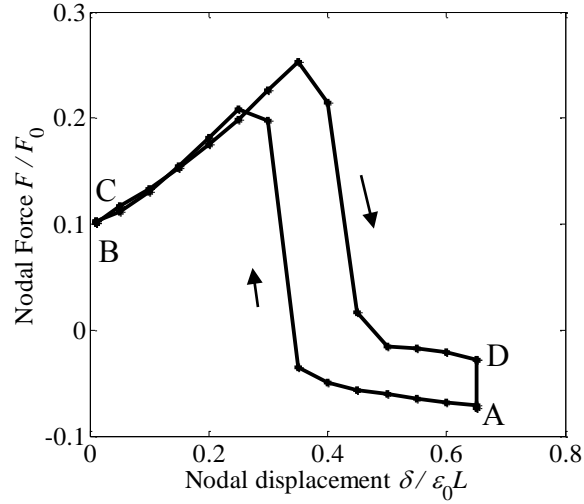
Figure 9: Plot of nodal forces and displacements on 'S' at $(x_1, x_2) = (40\text{nm}, 0)$ of the periodic cell, during the energy harvester cycle. Labels A-D corresponds to the harvester states in figure 7.

$\Delta\delta_i$ is thus greatest for nodes near $x_1 \rightarrow L$, and least for nodes at $x_1 \rightarrow 0$. Figure 9 shows the nodal force and displacement values at the node $(x_1, x_2) = (40\text{nm}, 0)$. Sharp transitions observed in figure 8(b) correspond with the changes in figure 9, which is caused by a domain wall sweeping across the corner of the periodic cell at $(x_1, x_2) = (40\text{nm}, 0)$.

The net electrical work output, from the voltage-charge curve, is ~0.04J/m^2 in each cycle. If operated at frequency 1kHz, a power density of ~40W/m^2 could be potentially generated, assuming ideal conditions. Since the external harvesting circuit in this design is required to carry out voltage switching at a frequency matching the driving oscillations, it is anticipated that the device would be designed with a macroscopic resonance frequency matching the available mechanical energy source. Suitable harvesting circuits have been designed for similar applications [38], [39]. Limitation of the substrate strain to safe operating levels could be practically achieved by blocking macroscopic oscillations greater than the limiting amplitude.

It is of interest to compare the power density achieved by the proposed device with that of other energy harvesting technologies. A wide range of mechanical energy harvesters has been developed in recent years, including piezoelectrics [18], [40]–[42], nanowire arrays [43]–[49], triboelectric devices [50]–[52] and magnetostrictives [53]–[55]. Power densities are commonly

expressed in terms of power per unit volume of working material at an operating frequency. Alternatively, for comparison with area based technologies such as photovoltaics, an area power density can be derived by factoring in the thickness of working material. Considering the well-established piezoelectric energy harvesters, cantilever devices such as that of Shen et al. [42] typically offer area power density of 0.2-0.3W/m^2 at around 200Hz. At this frequency, the proposed device could generate around 7W/m^2. The enhancement of more than an order of magnitude is due to the use of ferroelectric switching in place of piezoelectric response. Devices based on the bending of a nanowire array [43]–[49] appear to result in a wide range of power densities depending on the choice of material and operating regime. At the upper end of performance [45], [46], [48] the power density is comparable to that of the proposed ferroelectric harvester. The power generated by energy harvesters based on the concept of triboelectricity that uses contact electrification between the thin films of a polymer and a metal foil [50] can reaches up to 30-40W/m^2 at an operating frequency of 10Hz. This power density is about 100 times greater than the thin film ferroelectric energy harvester concept operating at the same frequency. By contrast, magnetostrictive energy harvesters such as that of Wang and Yuan [53] can achieve power densities around tens of mW/m^2, and so are better suited to applications requiring low power density. Finally it is worth noting that ground based solar photovoltaics which offer ~10% energy conversion efficiency [56]–[58], commonly achieve power densities of around 30-50W/m^2, which is similar to the proposed ferroelectric device operating at 1kHz.

5. Conclusion

A phase-field model has been employed to identify stable domain patterns and to explore the concept of an energy harvester device. A stripe domain pattern with in-plane polarizations was found to be stable over a wide range of externally imposed strains and its potential application in a conceptual thin film energy harvester device was demonstrated. The results indicate the energy harvester generates about 0.04J/m^2 on each cycle under ideal conditions such as assuming no losses in the energy harvesting circuitry. The device thus has power generation capability that compares favourably with a range of energy harvesting technologies, provided sufficient vibration energy is

available at its operating frequency. The work also illustrates a potential use of the phase-field model as a design tool in domain engineering of nanoscale devices.

Acknowledgements

References

[1] A. F. Devonshire, "Theory of ferroelectrics," *Adv. Phys.*, **3**, pp. 85–130, 1954.

[2] Q. Zuo, L. Luo, and Y. Yao, "The electrical , upconversion emission , and temperature sensing ferroelectric ceramics," **632**, pp. 711–716, 2015.

[3] J. F. Scott, "Applications of modern ferroelectrics," *Science (80-.).*, **315**, pp. 954–9, Feb. 2007.

[4] G. Park, C. R. Farrar, M. D. Todd, W. Hodgkiss, and T. Rosing, "Energy Harvesting for Structural Health Monitoring Sensor Networks," *Los Alamo*, **14**, no. 1, pp. 1–88, 2008.

[5] I. Münch, M. Krauß, C. M. Landis, and J. E. Huber, "Domain engineered ferroelectric energy harvesters on a substrate," *J. Appl. Phys.*, **109**, no. 2011, p. 104106, 2011.

[6] G. Sebald, S. Pruvost, and D. Guyomar, "Energy harvesting based on Ericsson pyroelectric cycles in a relaxor ferroelectric ceramic," *Smart Mater. Struct.*, **17**, p. 015012, 2008.

[7] I. I. Naumov, L. Bellaiche, and H. Fu, "Unusual phase transitions in ferroelectric nanodisks and nanorods.," *Nature*, **432**, no. 7018, pp. 737–40, Dec. 2004.

[8] Z. Hu, M. Tian, B. Nysten, and A. M. Jonas, "Regular arrays of highly ordered ferroelectric polymer nanostructures for non-volatile low-voltage memories.," *Nat. Mater.*, **8**, no. 1, pp. 62–67, 2009.

[9] Y. Kutes, L. Ye, Y. Zhou, S. Pang, B. D. Huey, and N. P. Padture, "Direct Observation of Ferroelectric Domains in Solution-Processed $CH_3NH_3PbI_3$ Perovskite Thin Films," *J. Phys. Chem. Lett.*, **5**, pp. 3335–3339, 2014.

[10] A. Kontsos and C. M. Landis, "Phase-Field Modeling of Domain Structure Energetics and Evolution in Ferroelectric Thin Films," *J. Appl. Mech.*, **77**, p. 041014, 2010.

[11] G. Arlt, "The role of domain walls on the dielectric, elastic and piezoelectric properties of ferroelectric ceramics," *Ferroelectrics*, **76**:1, pp. 451–458, 1987.

[12] P. C. Van Buskrik, J. F. Roeder, S. M. Bilodeau, M. W. Russell, S. T. Johnston, D. J. Vestyck, and T. H. Baum, "Scalable Lead Zirconium Titanate (PZT) Thin Film Material and Deposition Method, and Ferroelectric Memory Device Structures Comprising such Thin Film Material," *United States Pat.*, no. 19, 2013.

[13] A. Koka and H. A. Sodano, "Energy harvesting from arrays of long barium titanate nanowires," in *Proceedings of the ASME SMASIS 2013 conference*, 2013.

[14] E. K. H. Salje and J. F. Scott, "Ferroelectric Bloch-line switching: A paradigm for memory devices?," *Appl. Phys. Lett.*, **105**, p. 252904, 2014.

[15] J. Y. Li and D. Liu, "On ferroelectric crystals with engineered domain configurations," *J. Mech. Phys. Solids*, **52**, pp. 1719–1742, 2004.

[16] W. J. Chen, Y. Zheng, and B. Wang, "Phase field simulations of stress controlling the vortex domain structures in ferroelectric nanosheets," *Appl. Phys. Lett.*, **100**, no. 6, p. 062901, 2012.

[17] A. Koka and H. A Sodano, "High-sensitivity accelerometer composed of ultra-long vertically aligned barium titanate nanowire arrays.," *Nat. Commun.*, **4**, p. 2682, 2013.

[18] H. S. Kim, J. H. Kim, and J. Kim, "A review of piezoelectric energy harvesting based on vibration," *Int. J. Precis. Eng. Manuf.*, **12**, no. 6, pp. 1129–1141, 2011.

[19] L. Mazet, S. M. Yang, S. V Kalinin, S. Schamm-Chardon, and C. Dubourdieu, "A review of molecular beam epitaxy of ferroelectric $BaTiO_3$ films on Si, Ge and GaAs substrates and their applications," *Sci. Technol. Adv. Mater.*, **16**, no. 3, p. 036005, 2015.

[20] R. Ramesh and N. A Spaldin, "Multiferroics: progress and prospects in thin films," *Nat. Mater.*, **6**, pp. 21–29, 2007.

[21] N. Setter, D. Damjanovic, L. Eng, G. Fox, S. Gevorgian, S. Hong, A. Kingon, H. Kohlstedt, N. Y. Park, G. B. Stephenson, I. Stolitchnov, A. K. Taganstev, D. V. Taylor, T. Yamada, and S. Streiffer, "Ferroelectric thin films: Review of materials, properties, and applications," *J. Appl. Phys.*, **100**, no. 2006, pp. 1–46, 2006.

[22] S. Abel, M. Sousa, C. Rossel, D. Caimi, M. D. Rossell, R. Erni, J. Fompeyrine, and C. Marchiori, "Controlling tetragonality and crystalline orientation in $BaTiO_3$ nano-layers grown on Si," *Nanotechnology*, **24**, p. 285701, 2013.

[23] L. Mazet, R. Bachelet, L. Louahadj, D. Albertini, B. Gautier, R. Cours, S. Schamm-Chardon, G. Saint-Girons, and C. Dubourdieu, "Structural study and ferroelectricity of epitaxial $BaTiO_3$ films on silicon grown by molecular beam epitaxy," *J. Appl. Phys.*, **116**, no. 2014, p. 214102, 2014.

[24] R. G. P. McQuaid, L. J. McGilly, P. Sharma, A. Gruverman, and J. M. Gregg, "Mesoscale flux-closure domain formation in single-crystal $BaTiO_3$.," *Nat. Commun.*, **2**, no. May, p. 404, Jan. 2011.

[25] Y. Ivry, D. P. Chu, J. F. Scott, and C. Durkan, "Flux Closure Vortexlike Domain Structures in Ferroelectric Thin Films," *Phys. Rev. Lett.*, **104**, no. 20, p. 207602, May 2010.

[26] J. M. Gregg, "Exotic Domain States in Ferroelectrics: Searching for Vortices and Skyrmions," *Ferroelectrics*, **433**, no. 1, pp. 74–87, Jan. 2012.

[27] N. Balke, B. Winchester, W. Ren, Y. H. Chu, A. N. Morozovska, E. A. Eliseev, M. Huijben, R. K. Vasudevan, P. Maksymovych, J. Britson, S. Jesse, I. Kornev, R. Ramesh, L. Bellaiche, L. Q. Chen, and S. V. Kalinin, "Enhanced electric conductivity at ferroelectric vortex cores in BiFeO$_3$," *Nat. Phys.*, **8**, no. 1, pp. 81–88, 2011.

[28] L.-Q. Chen, "Phase-Field Method of Phase Transitions/Domain Structures in Ferroelectric Thin Films: A Review," *J. Am. Ceram. Soc.*, **91**, no. 6, pp. 1835–1844, Jun. 2008.

[29] S. H. Baek, H. W. Jang, C. M. Folkman, Y. L. Li, B. Winchester, J. X. Zhang, Q. He, Y. H. Chu, C. T. Nelson, M. S. Rzchowski, X. Q. Pan, R. Ramesh, L. Q. Chen, and C. B. Eom, "Ferroelastic switching for nanoscale non-volatile magnetoelectric devices," *Nat. Mater.*, **9**, no. April, pp. 309–314, 2010.

[30] J. Wang and T. Y. Zhang, "Phase field simulations of polarization switching-induced toughening in ferroelectric ceramics," *Acta Mater.*, **55**, pp. 2465–2477, 2007.

[31] K. Dayal and K. Bhattacharya, "A real-space non-local phase-field model of ferroelectric domain patterns in complex geometries," *Acta Mater.*, **55**, pp. 1907–1917, 2007.

[32] Y. Su and C. M. Landis, "Continuum thermodynamics of ferroelectric domain evolution: Theory, finite element implementation, and application to domain wall pinning," *J. Mech. Phys. Solids*, **55**, pp. 280–305, Feb. 2007.

[33] A. Kontsos and C. M. Landis, "Computational modeling of domain wall interactions with dislocations in ferroelectric crystals," *Int. J. Solids Struct.*, **46**, pp. 1491–1498, Mar. 2009.

[34] N. T. Tsou, P. R. Potnis, and J. E. Huber, "Classification of laminate domain patterns in ferroelectrics," *Phys. Rev. B - Condens. Matter Mater. Phys.*, **83**, no. 184120, pp. 1–6, 2011.

[35] A. Renuka Balakrishna, I. Muench, and J. E. Huber, "Study of periodic domain patterns in tetragonal ferroelectrics using phase-field methods," in *Proceedings of the ASME SMASIS 2015 conference*, 2015, pp. 1–6.

[36] J. Muñoz-Saldaña, G. A. Schneider, and L. M. Eng, "Stress induced movement of ferroelastic domain walls in BaTiO3 single crystals evaluated by scanning force microscopy," *Surf. Sci.*, vol. 480, 2001.

[37] V. Nagarajan, A. Roytburd, A. Stanishevsky, S. Prasertchoung, T. Zhao, L. Chen, J. Melngailis, O. Auciello, and R. Ramesh, "Dynamics of ferroelastic domains in ferroelectric thin films.," *Nat. Mater.*, vol. 2, no. January, pp. 43–47, 2003.

[38] D. Guyomar, A. Badel, E. Lefeuvre, and C. Richard, "Toward energy harvesting using active materials and conversion improvement by nonlinear processing," *IEEE Trans. Ultrason. Ferroelectr. Freq. Control*, vol. 52, no. 4, pp. 584–594, 2005.

[39] H. K. H. Kim, S. Priya, H. Stephanou, and K. Uchino, "Consideration of Impedance Matching Techniques for Efficient Piezoelectric Energy Harvesting," *IEEE Trans. Ultrason. Ferroelectr. Freq. Control*, vol. 54, no. 9, pp. 1851–1859, 2007.

[40] A. Mathers, K. S. Moon, J. Yi, and S. Member, "A Vibration-Based PMN-PT Energy Harvester," vol. 9, no. 7, pp. 731–739, 2009.

[41] H. Liu, C. Lee, T. Kobayashi, C. J. Tay, and C. Quan, "Piezoelectric MEMS-based wideband energy harvesting systems using a frequency-up-conversion cantilever stopper," *Sensors Actuators A Phys.*, vol. 186, pp. 242–248, 2012.

[42] D. Shen, J. H. Park, J. H. Noh, S. Y. Choe, S. H. Kim, H. C. Wikle, and D. J. Kim, "Micromachined PZT cantilever based on SOI structure for lowfrequency vibration energy harvesting," *Sensors Actuators, A Phys.*, vol. 154, pp. 103–108, 2009.

[43] J. Briscoe and S. Dunn, "Piezoelectric nanogenerators – a review of nanostructured piezoelectric energy harvesters," *Nano Energy*, vol. 14, pp. 15–29, 2015.

[44] S. Xu, Y. Qin, C. Xu, Y. Wei, R. Yang, and Z. L. Wang, "Self-powered nanowire devices.," *Nat. Nanotechnol.*, vol. 5, no. 5, pp. 366–373, 2010.

[45] S. Xu, B. J. Hansen, and Z. L. Wang, "Piezoelectric-nanowire-enabled power source for driving wireless microelectronics.," *Nat. Commun.*, vol. 1, no. 7, p. 93, 2010.

[46] J. Briscoe, M. Stewart, M. Vopson, M. Cain, P. M. Weaver, and S. Dunn, "Nanostructured p-n junctions for kinetic-to-electrical energy conversion," *Adv. Energy Mater.*, vol. 2, pp. 1261–1268, 2012.

[47] A. Koka, Z. Zhou, and H. A. Sodano, "Vertically aligned BaTiO $_3$ nanowire arrays for energy harvesting," *Energy Environ. Sci.*, vol. 7, pp. 288–296, 2014.

[48] X. Chen, S. Xu, N. Yao, and Y. Shi, "1.6 V Nanogenerator for Mechanical Energy Harvesting Using PZT Nanofibers," *Nano Lett.*, vol. 10, pp. 2133–2137, 2010.

[49] W. Wu, S. Bai, M. Yuan, Y. Qin, Z. L. Wang, and T. Jing, "Lead zirconate titanate nanowire textile nanogenerator for wearable energy-harvesting and self-powered devices," *ACS Nano*, vol. 6, no. 7, pp. 6231–6235, 2012.

[50] S. Wang, L. Lin, and Z. L. Wang, "Nanoscale-triboelectric-effect enabled energy conversion for sustainable powering of portable electronics," *Nano Lett.*, vol. 12, pp. 6339–46, 2012.

[51] J. Chen, G. Zhu, W. Yang, Q. Jing, P. Bai, Y. Yang, T. C. Hou, and Z. L. Wang, "Harmonic-resonator-based triboelectric nanogenerator as a sustainable power source and a self-powered active vibration sensor," *Adv. Mater.*, vol. 25, pp. 6094–6099, 2013.

[52] L. Lin, S. Wang, Y. Xie, Q. Jing, S. Niu, Y. Hu, and Z. L. Wang, "Segmentally structured disk triboelectric nanogenerator for harvesting rotational mechanical energy," *Nano Lett.*, vol. 13, pp. 2916–2923, 2013.

[53] L. Wang and F. G. Yuan, "Vibration energy harvesting by magnetostrictive material," *Smart Mater. Struct.*, vol. 17, p. 045009, 2008.

[54] Y. Zhu and J. W. Zu, "From the Vibration of Magnetic Levitation," vol. 48, no. 11, pp. 3344–3347, 2012.

[55] X. Dai, Y. Wen, P. Li, J. Yang, and M. Li, "Energy harvesting from mechanical vibrations using multiple magnetostrictive/piezoelectric composite transducers," *Sensors Actuators, A Phys.*, vol. 166, no. 1, pp. 94–101, 2011.

[56] B. O'Regan and M. Grätzel, "A low-cost, high-efficiency solar cell based on dye-sensitized colloidal TiO $_2$ films," *Nature*, vol. 353, pp. 737–740, 1991.

[57]   J. You, L. Dou, K. Yoshimura, T. Kato, K. Ohya, T. Moriarty, K. Emery, C.-C. Chen, J. Gao, G. Li, and Y. Yang, "A polymer tandem solar cell with 10.6% power conversion efficiency.," *Nat. Commun.*, vol. 4, p. 1446, 2013.

[58]   D. A. R. Barkhouse, O. Gunawan, T. Gokmen, T. K. Todorov, and D. B. Mitzi, "Device characteristics of a 10.1% hydrazine-processed Cu2ZnSn(Se,S)4 solar cell," *Prog. Photovoltaics Res. Appl.*, vol. 20, no. Version 45, pp. 6–11, 2012.